Inorganic Chemistry

pubs.acs.org/IC Article

Cycloidal Magnetic Order Promoted by Labile Mixed Anionic Paths in $M_2(SeO_3)F_2$ (M = Mn^{2+}, Ni^{2+})

Tianyu Zhu, Olivier Mentré,* Haoming Yang, Yong Jin, Xinan Zhang, Ángel M. Arévalo-López, Clemens Ritter, Kwang-Yong Choi, and Minfeng Lü*

Cite This: https://doi.org/10.1021/acs.inorgchem.1c01074 Read Online

ACCESS | Metrics & More | Article Recommendations | Supporting Information

ABSTRACT: Two $M_2(SeO_3)F_2$ fluoro-selenites (M = Mn^{2+}, Ni^{2+}) have been synthesized using optimized hydrothermal reactions. Their 3D framework consists of 1D-$[MO_2F_2]^{4-}$chains of edge-sharing octahedra with a rare topology of alternating O−O and F−F μ_2 bridges. The interchain corner-sharing connections are assisted by the mixed O vs F anionic nature and develop a complex set of M−X−M superexchanges as calculated by LDA+U. Their interplay induces prominent in-chain antiferromagnetic frustration, while the interchain exchanges are responsible for the cycloidal magnetic structure observed below $T_N \approx 21.5$ K in the Ni^{2+} case. For comparison the Mn^{2+} compound develops a nearly collinear spin (canted) ordering below $T_N \approx 26$ K with ferromagnetic chain units.

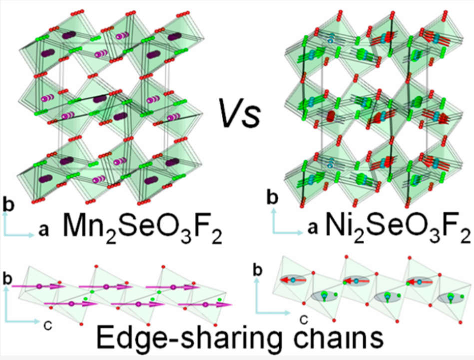

1. INTRODUCTION

Compounds with multiple anions have received great interest from inorganic solid-state chemists due to heteroanionic characteristics, adding new dimensions to the electronic structure, which may support physical phenomena inaccessible to a single-anion analogue, including competition between labile magnetic exchanges.[1] Recently, multiple anion ideas have been extended to the oxy-halide system M−L−O−X (M = metal cation, L = p-block lone-pair elements such as Te^{4+}, Se^{4+}, X = halide anion). It is common that the role of lone-pair cations on selenites as chemical scissors help to form low-dimensional framework materials. Halide insertion leads to two categories: the larger halide ions (Cl^- and Br^-) are inclined to generate extended nonbonding regions when they interact with lone-pair elements so that the two-dimensional (2D) structure is often adopted (see $Cu_5(SeO_3)_4Cl_2$[2]). On the other hand, the smaller fluoride anion may act as a bridging species between transition-metal cations, forming there by sizable dimensionalities in phases such as the 1D-$Fe(SeO_3)F$[3] or the 3D-$M_2(SeO_3)F_2$ (M = Co, Cu).[4,5] Here, the contrasting magnetic exchanges mediated by O^{2-} vs F^- may create a playground for destabilizing the standard collinear spin order into exotic orders and provide a nice platform for spin-induced multiferroicity.[6] Only few examples of selenium oxofluorides have been reported due to difficult control of the reactive fluorine ions[7−9] using HF (or others) as a dual mineralizer and strong acid suitable for the formation of metal ions. In fact, reacting SeO_2, a metal halide, and the acid HF is a suitable strategy to grow single crystals of $M_2(SeO_3)F_2$ (M = Co, Cu).[4,5] The realization of polycrystalline mixed $(Mn,Zn)_2(SeO_3)F_2$ by fine adjustment of the pH environment using NH_4OH was achieved, but the crystal growth was hampered by the reduction of Se(IV) to Se(0) above 120 °C,[10] which remains a chemical challenge. Similarly, powdered samples of $M_2(SeO_3)F_2$ (M = Mn, Co, Ni) have first been achieved via hydrothermal techniques. The crystal structures of $M_2(SeO_3)F_2$ (M = Mn, Ni) were then solved by powder diffraction until single crystals of isostructural $Co_2(SeO_3)F_2$ were obtained by chemical transport reactions.[11] In this work, we report the preparation, single-crystal growth, and structures of the $M_2(SeO_3)F_2$ (M = Mn, Ni) analogues. Although several $M^{2+}{}_2(SeO_3)F_2$ species have been reported, their full magnetic characterization has not. We probe here versatile magnetic exchanges scaled by M−X−M paths, which return a nearly collinear (M = Mn) versus cycloidal (M = Ni) magnetic structure analyzed by means of *ab initio* calculations and neutron diffraction.

2. EXPERIMENTAL SECTION

2.1. Synthesis. Powdered $M_2(SeO_3)F_2$ (M = Mn, Co, Ni) compounds can be achieved by HF as a mineralizer under hydrothermal conditions. However, an environment having too low a pH value is not suitable for the formation of single crystals. We

Received: April 7, 2021

introduced hydrazine to enhance the pH of the hydrothermal solutions and to obtain single crystals of $Mn_2(SeO_3)F_2$. To recover single crystals of $Ni_2(SeO_3)F_2$, we introduced KOH to adjust the pH of the hydrothermal solutions. Our $Mn_2SeO_3F_2$ (**I**) and $Ni_2SeO_3F_2$ (**II**) compounds were obtained as single crystals and powdered samples, as detailed in the Supporting Information.

2.2. Characterization. The SCXRD data of all the investigated samples have been collected using a Bruker SMART APEX II diffractometer with a 1K CCD area detector and monochromated Mo Kα radiation (λ = 0.71073 Å) at room temperature. To acquire the data, a narrow-frame method was used with scan widths of 0.30° in ω and an exposure time of 10 s/frame. Integration of the obtained data has been performed via the program SAINT.[12] Absorption corrections have been carried out by the multiscan method using the program SADABS.[13] The crystallographic data for both of the reported compounds are given in Table 1. The CCDC deposition numbers are 2046139 and 2046140 for $Mn_2SeO_3F_2$ and $Ni_2SeO_3F_2$, respectively. The refined anisotropic displacement parameters and atomic coordinates are summarized in the Supporting Information. The pertinent distances and angles are given in Tables S3 and S6.

Table 1. Crystal Data, Measurement Parameters, and Structural Refinement Parameters of $M_2SeO_3F_2$ (M = Mn, Ni) at Room Temperature

	$Mn_2SeO_3F_2$	$Ni_2SeO_3F_2$
molar mass (g/mol)	274.8	282.3
symmetry	orthorhombic	orthorhombic
space group	*Pnma*	*Pnma*
a (Å)	7.4958(3)	7.1727(5)
b (Å)	10.3382(4)	9.9377(7)
c (Å)	5.4717(2)	5.2364(4)
V (Å^3)	424.02(3)	373.25(5)
μ (mm^{-1})	14.481	19.773
R(int) (%)	4.34	7.74
no. of indep rflns all ($I > 3\sigma(I)$)	554	488
no. of indep rflns obsd ($I > 3\sigma(I)$)	452	359
no. of refined params	40	40
$R(F)^a$ ($I > 3\sigma(I)$/all data, %)	3.27/4.09	3.36/5.22
$R_w(F^2)^b$ ($I > 3\sigma(I)$/all data, %)	4.38/4.45	3.64/3.85
max/min residual electronic density (e/Å^3)	0.86/−2.00	1.00/−1.11

$^aR = \sum||F_o| - |F_c||/\sum|F_o|$. $^bR_w = [\sum w(|F_o{}^2| - |F_c{}^2|)^2/\sum w|F_o{}^2|^2]^{1/2}$, $w = 1/(\sigma^2(F_o{}^2) + (0.0682P)^2)$ with $P = (\max(F_o{}^2, 0) + 2F_c{}^2)/3$.

PXRD patterns were collected using a Bruker D8 Advance X-ray powder diffractometer with Cu Kα radiation (λ = 1.54056 Å, 40 kV/40 mA). The XRD powder patterns shown in Figure 1 match well the calculated patterns using the model obtained from the single-crystal data reported.

Energy-dispersive analysis by X-ray (EDAX) of the isolated blue crystals was carried out using a Phenom ProX desktop analyzer. Infrared spectra for the reported materials were recorded on a Varian 670-IR FTIR spectrometer. As the synthesis route can introduce hydroxyl groups instead of fluorine ions, the presence of fluorine was verified by EDX analysis (Figures S1 and S2) and the absence of OH groups at around 3500 cm^{-1} by IR spectroscopy (Figure S3). X-ray photoelectron spectroscopy (XPS) measurements were performed using a Thermo Scientific K-Alpha$^+$ instrument. Thermogravimetric analysis (TGA) was performed using a thermal gravimetric analyzer (Model TGA5500, TA Instruments). Detailed experimental information is provided in Figures S4−S7 in the Supporting Information.

The DC magnetic susceptibilities for polycrystalline $Mn_2SeO_3F_2$ and $Ni_2SeO_3F_2$ were measured with a commercial Quantum Design Physical Properties Measurement System (PPMS). Zero-field-cooled (ZFC) and field-cooled (FC) data were recorded within the temperature range of 2−400 K with an external field of 1000 Oe. Isothermal magnetization curves were collected in a field range of −9 to +9 T.

The specific heat measurements were collected with the heat capacity option of a physical properties measurement system (PPMS-9, Quantum Design).

Neutron powder diffraction (NPD) data were collected on the high-intensity powder diffractometer D20 at the Institut Laue Langevin (ILL), Grenoble, France. Long acquisitions of 5 h were carried out at 1.5 and 30 K for $Ni_2SeO_3F_2$. The thermal dependence between 2 and 30 K was studied using shorter runs of 15 min, taking spectra about every 0.7 K. This thermodiffractogram confirmed that all magnetic Bragg peaks appear at the same temperature and show a similar temperature dependence, thereby indicating the presence of a single magnetic propagation vector. High-resolution data on the Ni compound were taken at 2 K on the D2B diffractometer, as well at the ILL, with λ = 1.594 Å and confirmed the persistence of the *Pnma* structure. $Mn_2SeO_3F_2$ was measured at 1.5 and 30 K on the D20 diffractometer using 30 min runs. NPD patterns were refined by the Rietveld method using the program FULLPROF.[14]

2.3. DFT Calculations. Density functional theory (DFT) band structure calculations were performed using the full-potential local-orbital scheme (FPLO9.00-33).[15] Applying the local density approximation (LDA+U, U = 3.6) with the exchange-correlation potential by Perdew and Wang[16] using the Vienna *ab initio* simulation package (VASP)[17] with the basis set of projected augmented waves;[18] we mapped the total energies for a number of collinear spin configurations into a classical Heisenberg model to yield individual exchange couplings for U = 4.6 eV and the effective on-site exchange interaction J_{eff} = 1 eV. The set of magnetic configurations used to deduce the main exchange values is given in Figure S13 together with the details of their energies.

3. RESULTS AND DISCUSSION

Both of the reported compounds $Mn_2(SeO_3)F_2$ (a = 7.4958(3)Å, b = 10.3382(4)Å, c = 5.4717(2)Å, Z = 4, R_F = 3.27%) and $Ni_2(SeO_3)F_2$ (a = 7.1727(5)Å, b = 9.9377(7)Å, c = 5.2364(4)Å, Z = 4, R_F = 3.36%) crystallize in the orthorhombic space group *Pnma* and are isomorphous with $M_2(XO)_3F_2$ (M = Co, Cu, Mn and X = Te, Se).[4,5,10] Note that our single-crystal XRD data allow for a more accurate structural model than has been reported for the Mn and Ni compounds, which was necessary for the DFT calculations initiated later. A significant but isotropic contraction of all lattice parameters by ∼5% occurs for $Ni_2(SeO_3)F_2$ related to the Mn^{2+} vs Ni^{2+} relative ionic radii, which highlights the three-dimensional (3D) character of the framework.

The Mn/Ni coordination is a distorted MO_3F_3 octahedron, with distances being given in Tables S3 and S6 in the Supporting Information, all oxygens being shared by $(SeO_3)_2$ trigonal-pyramidal groups, where the stereochemically active selenium lone pair completes a distorted tetrahedron. As described before,[5] the crystal structure of $M_2SeO_3F_2$ is composed of $[MO_3F_3]$ octahedra and SeO_3 trigonal pyramids. An isostructural description has been established for $Mn_2SeO_3F_2$, as detailed in Figure S8 in the Supporting Information. Rather than the description of the dense 3D packing used for the parent $Co_2(TeO)_3F_2$,[5] we will refer here to the assembly of 1D subunits already pointed out in the (Zn,Mn) case,[10] which is much better suited to the decoding of the magnetic properties detailed below. Here one should focus on the most dense 1D zigzag chains formed by edge sharing along the c axis of alternating O−O and F−F μ_2 bridges, creating a rare situation reported only for $Na_2Fe(PO_4)F$[19] and $Fe(SeO_3)F$,[3] to the best of our knowledge. The individual edge-sharing chains are highlighted in Figure 2a,b for clarity. These chains share all of their O and F corners apart

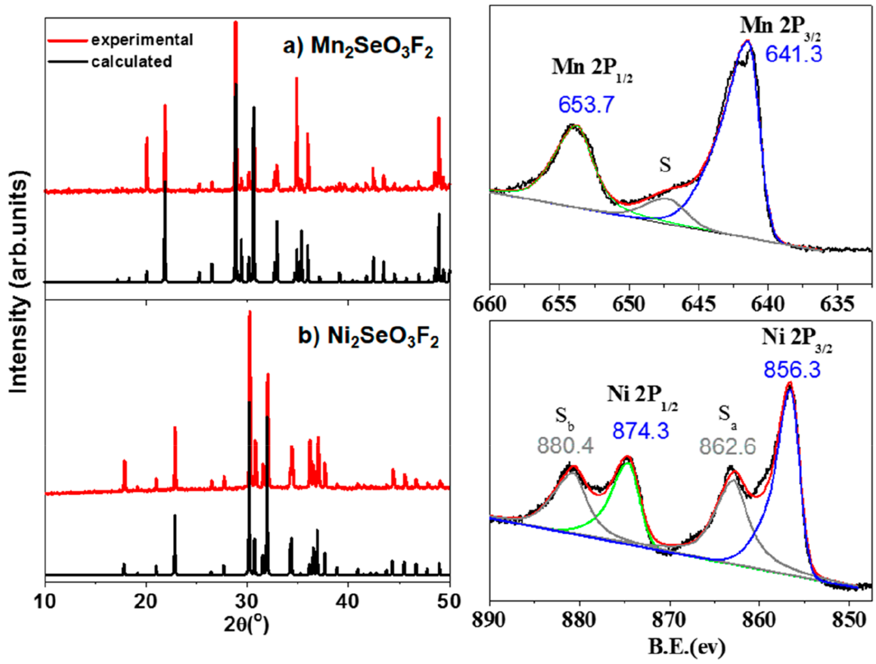

Figure 1. X-ray powder patterns of the experimental studies (red) and calculation from the single crystal XRD data (black) and Mn/Ni 2p XPS data for (a) $Mn_2SeO_3F_2$ and (b) $Ni_2SeO_3F_2$.

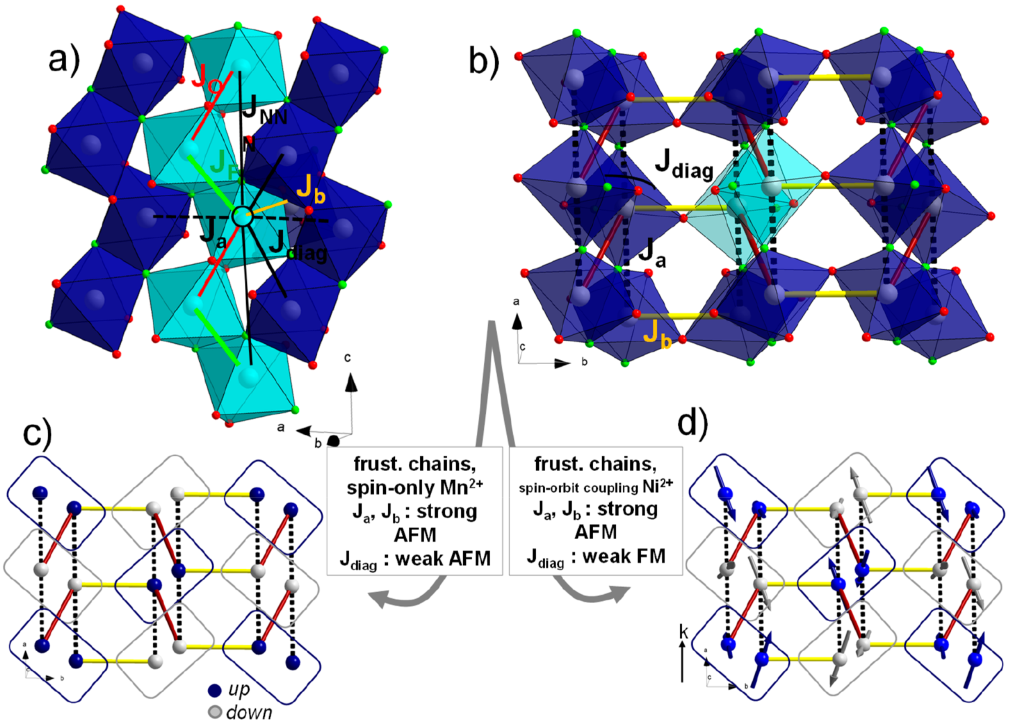

Figure 2. $M_2(SeO_3)F_2$ crystal structure and labels of the main magnetic exchanges. (a, b) Interchain connections for two projections in the *a,c* and *a,b* planes. O and F shown are in red and green, respectively. The pale blue units allow distinguishing an edge-sharing chain from its (dark blue) neighbors. (c, d) Projected magnetic structures for (c) M = Mn and (d) M = Ni, where the rectangles show the projected edge-sharing chains.

from the edge-sharing O_2 bridges with surrounding chains, leaving a dense 3D lattice projected in the *a,b* plane in Figure 2b. The bases of the chains are parallel along the *a* axis and are tilted by ∼110°, leading to nearly triangular channels occupied by the Se^{4+} ions. Bond valence sum calculations[20] for Mn^{2+} ($\sum S_i = 1.98(1)$) and Ni^{2+} ($\sum S_i = 1.96(1)$) confirm divalent metal states and tetravalent Se^{4+}cations and allow the clear distinction of O^{2-} against F^- sites (see Table S7).

The Mn(II) and Ni(II) and heterocoordination were further confirmed by XPS spectroscopy. The shape and position of the Mn 2p core level indicate the divalent Mn oxidation state that is also characterized by its intense "shake-up" satellite, approximately 6 eV below the main 2p peaks, shown in Figure 1a. The binding energy of the Mn $2p_{3/2}$ peak centered at 641.3 eV is consistent with those found for MnO (640.9 eV[21]) and MnF_2 (642.4 eV[22]). Since there is one crystallographically

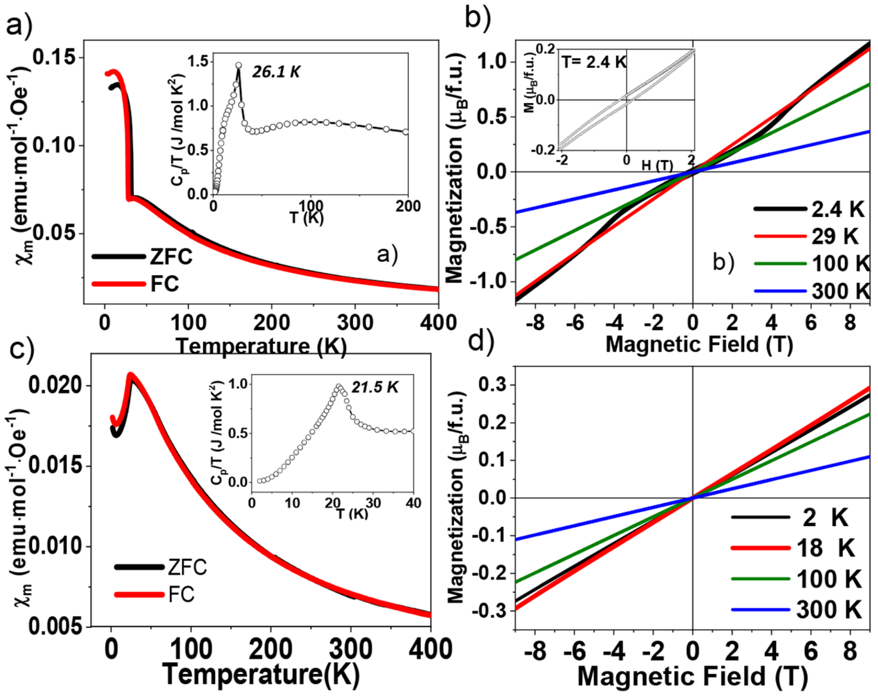

Figure 3. FC and ZFC curves of (a) $Mn_2SeO_3F_2$ and (c) $Ni_2SeO_3F_2$. The insets show the specific heat divided by the temperature $C_p(T)/T$ between 2 and 300 K. Field dependence of magnetization taken between 2.4 and 300 K of (b) $Mn_2SeO_3F_2$ and (d) $Ni_2SeO_3F_2$. The inset for (c) shows an enlarged view of the low-field range at 2.4 K.

Table 2. Basis Vectors S_x, S_y, and S_z and the Associated Irreducible Presentation Γ_i Associated with the Equivalent Positions for the Magnetic Structures of $M_2(SeO_3)F_2$ (M= Mn, Ni) Compounds

	M = Mn (M_z = 4.34(1) μ_B)		M = Ni (M_x = −1.82(5), M_y = 0.6(1), M_z = −1.77(5) μ_B)	
coordinates	S_z: $\Gamma_{5,z}$ real	S_x: $\Gamma_{3,x}$ imaginary	S_y: $\Gamma_{4,y}$ imaginary	S_z: $\Gamma_{2,z}$ real
		Orbital 1		
x, y, z	$+m_z$	0	0	$+m_z$
$x + 1/2, -y + 1/2, -z + 1/2$	$+m_z$	$-m_x \sin k\pi$	$-m_y \sin k\pi$	$+m_z \sin k\pi$
$x + 1/2, y, -z + 1/2$	$-m_z$	$+m_x \cos k\pi$	$-m_y \cos k\pi$	$-m_z \cos k\pi$
$x, -y + 1/2, z$	$-m_z$	0	0	$-m_z$
		Orbital 2		
$-x + 1/2, -y, z + 1/2$	$-m_z$	0	0	$+m_z$
$-x, y + 1/2, -z$	$-m_z$	$-m_x \sin k\pi$	$-m_y \sin k\pi$	$+m_z \sin k\pi$
$-x, -y, -z$	$+m_z$	$+m_z \cos k\pi$	$-m_y \cos k\pi$	$-m_z \cos k\pi$
$-x + 1/2, y + 1/2, z + 1/2$	$+m_z$	0	0	$-m_z$

unique Mn atom, the $2p_{3/2}$ peak centered at 641.3 eV is intermediate between that for MnF_2 (642.4 eV) and that for MnO (640.9 eV), supporting the mixed anionic Mn coordination.

The valence state of the Mn(II) ion was further confirmed by the magnitude of the exchange splitting of the core-level spectra of Mn 3s. More specifically, one peak splits into two due to the exchange interaction between the Mn 3s and Mn 3d electrons.[22] The Mn 3s splitting value for **I** is approximately 6.3 eV, as shown in Figure S5, which is consistent with the value of 6.3 eV for MnF_2[21] and 5.8 eV for MnO.[23]

The XPS Ni 2p patterns of **II** are also shown in Figure 1b, and the typical Ni $2p_{3/2}$, Ni $2p_{1/2}$ and satellite (s) peaks are indicated. Similarly, the most intense peak, at around 856.3 eV, is intermediate between that for NiF_2 (858.1 eV) and that for NiO (853.8 eV),[24] in good agreement with Ni^{2+} in its NiO_3F_3 octahedron.

The magnetic susceptibility of $Mn_2SeO_3F_2$ is similar to that reported in ref 10. In a few words, it shows a ZFC/FC divergence below T_N = 26.1(1) K. The Curie−Weiss fit above 100 K results in a Curie−Weiss temperature (Θ_{CW}) = −71.0(1) K and μ_{eff} = 5.88(2) μ_B per Mn^{2+} (see Figure S9, vs 6.06 μ_B/Mn^{2+} in ref 10), close to the spin-only value of 5.92 μ_B (S = 5/2, L = 0, g = 2), similarly to other Mn^{2+} fluorophosphates such as $(NH_4)Mn_3(PO_3F)_2(PO_2F_2)F_2$[7] and $Ba_2Mn_2(PO_3F)F_6$.[25] Figure 3b shows the isothermal magnetization $M(H)$ at various temperatures, which reaches $M_{9T} \approx$ 1.17 μ_B/Mn^{2+} at 2.4 K. The aligned moment for our sample is also higher than that reported for polycrystals ($M_{12T} \approx$ 0.84 μ_B/Mn^{2+}).[10] A clear hysteresis with a coercive field of ~0.2 T and a remnant moment of ~0.012 μ_B/Mn^{2+} is assigned to a canting angle at zero field of $\sin^{-1}(0.012/5)° = 0.13°$ assuming 5 μ_B/Mn^{2+}. This phenomenon is further enhanced above the field-induced metamagnetic transition centered at μ_0H = 4 T. Here a canting angle of θ = 2.87° at 9 T can be estimated after

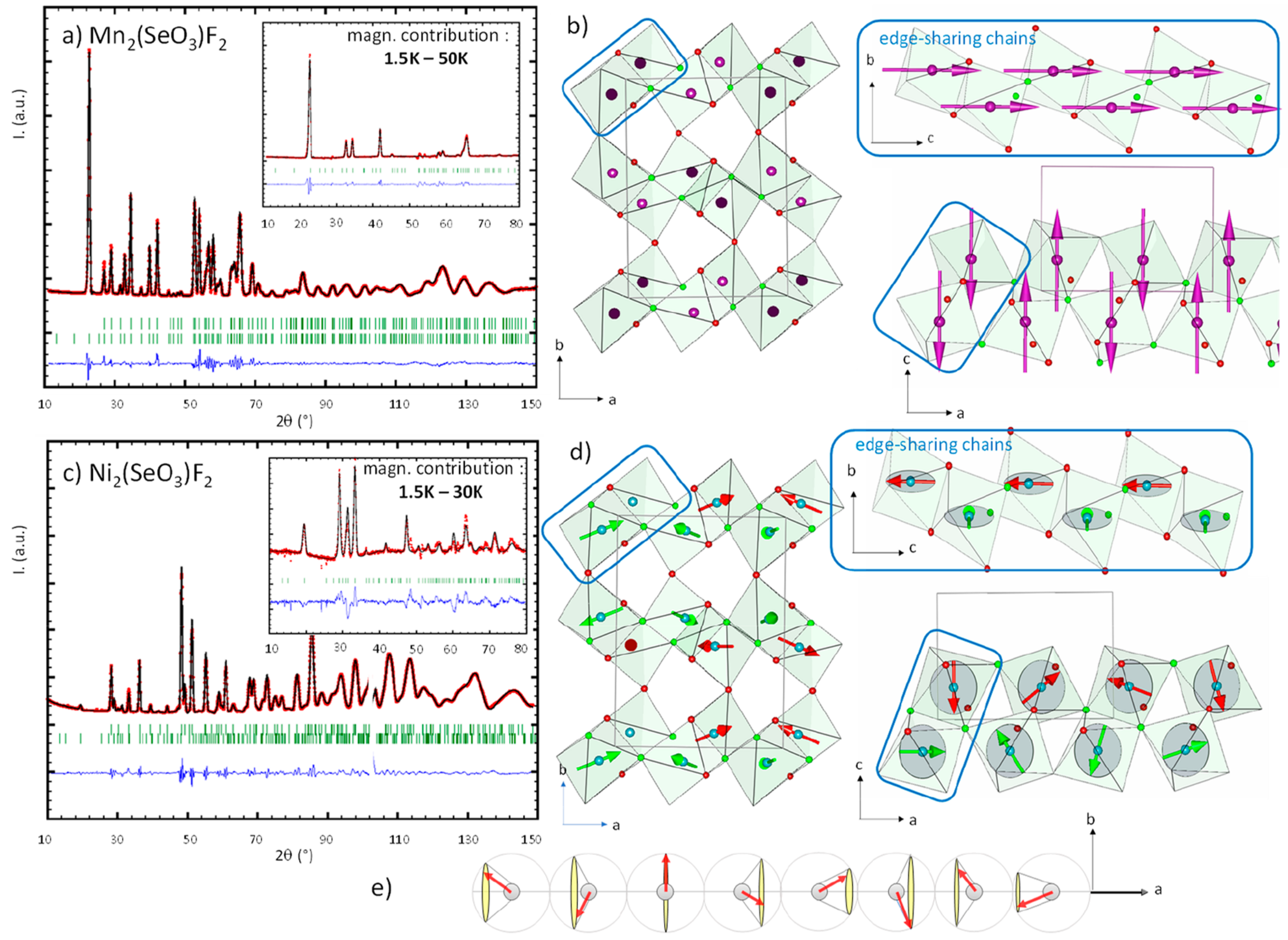

Figure 4. PND Rietveld refined patterns at 1.5 K (the AFM−paramagnetic difference is given in the inset) and refined magnetic models for (a, b) $Mn_2(SeO_3)F_2$ and (c, d) $Ni_2(SeO_3)F_2$. (e) Scheme of the magnetic cycloid along the *a* axis in the latter.

subtracting the linear AFM $M(H)$ component. Given the absence of symmetry centers in the main inter- and intrachains superexchange paths (see below), Dzyaloshinki−Moriya effects can plausibly explain such a spin-canted phenomenon.

Figure 3c shows no significant ZFC/FC divergence for $Ni_2SeO_3F_2$; thus, the onset of AFM ordering occurs below $T_N = 21.7(1)$ K. This is supported also by the λ-shaped anomaly observed in specific heat measurements (see the inset of Figure 3c). The Curie−Weiss fit above T_N returns $\Theta_{CW} = -100.9(1)$ K and $\mu_{eff} = 3.37(1)\ \mu_B/Ni^{2+}$ (see Figure S11). The negative Θ_{CW} value suggests predominantly antiferromagnetic interactions between the Ni^{2+} ions. μ_{eff} is higher than the spin-only value of 2.82 μ_B, indicating a significant orbital contribution of Ni^{2+} in an octahedral environment, similar to the case for $Ni_3(TeO_3)(SO_4)(OH)_2 \cdot 2H_2O$.[26] $M(H)$ for $Ni_2SeO_3F_2$ is plotted in Figure 3d. It increases linearly with increasing field and reaches $M_{9T} = 0.13\ \mu_B/Ni^{2+}$ at 2 K, confirming robust AFM.

The magnetic structure of $Mn_2(SeO_3)F_2$ was solved and refined using powder neutron diffraction (PND) data collected at 1.5 K on the D20 diffractometer ($\lambda = 2.41$ Å) at the Institut Laue langevin (ILL), Grenoble, France. Magnetic contributions appear below T_N on nuclear contributions according to the propagation vector $k = [0,0,0]$, the main contributions violating the *Pnma* extinctions. A magnetic symmetry analysis using Basireps[14] indicates a decomposition of the Γ magnetic representation into eight irreducible representations of dimension 1, contained three times each in $\Gamma_{magn} = 3\Gamma_1 + 3\Gamma_2 + 3\Gamma_3 + 3\Gamma_4 + 3\Gamma_5 + 3\Gamma_6 + 3\Gamma_7 + 3\Gamma_8$. Only the representation Γ_5 leads to a good agreement between experimental and calculated intensities, using the M_z contribution only (M_x, $M_y = 0$) (see Table 2). The refinement of the magnetic contribution pattern ($T_{1.5K} - T_{50K}$) yields $R_{magn} = 12.7\%$ and $M_{Mn^{2+}} = 4.34(1)\ \mu_B$. The magnetic structure consists of ferromagnetic collinear edge-sharing chains running along *z*, AFM coupled by corner sharing along the *x* and *y* axes.

The situation is far different in dealing with $Ni_2(SeO_3)F_2$, where combined high-resolution D1B and high-intensity D20 data were necessary to identify an incommensurate propagation vector refined to $k = [0.303(1),0,0]$, which curiously remains temperature independent below T_N (see Figure S12). A group theory analysis splits Ni into two orbitals *x*, *y*, *z* and $-x + 1/2$, $-y$, $z + 1/2$, sharing the same decomposition of magnetic representations $\Gamma_{magn} = 3\Gamma_1 + 3\Gamma_2 + 3\Gamma_3 + 3\Gamma_4$. A combination of the imaginary and real parts of the last three has been used, and the results are given in Table 2. Then the magnetic structure could be treated by either a sinusoidal or a cycloidal spin ordering indistinguishable by PND. The sinusoidal wave returns a modulated spin amplitude, with an unrealistic maximum values of 2.6 μ_B for Ni^{2+} ($S = 1$). Thus,

Table 3. Magnetic Exchange Geometrical Parameters for Different Exchange Paths in $M_2(SeO_3)F_2$ (M= Mn, Ni)[a]

	$Mn_2(SeO_3)F_2$: T_N = 26.1 K, Θ_{CW} = −71.0(1) K				$Ni_2(SeO_3)F_2$: T_N = 21.7 K, Θ_{CW} = −100.9(1) K			
exchange type	Mn−Mn (Å)	Mn−X_{SE} (Å), X−X_{SSE} (Å)	Mn−X−M_{SE} (deg), Mn−X−X−Mn $_{SSE}$ (deg)	J/K_b (K)	Ni−Ni (Å), X−X_{SSE} (Å)	Ni−X (Å), N−X−X−Ni_{SSE} (deg)	Ni−X−Ni (deg)	J/K_b (K)
1 × J_O(M−O_2−M)	3.39	2.13, 2.24	101.8	2.74	3.16	2.02, 2.06	101.4	24.26
1 × J_F(M−F_2−M)	3.38	2.15, 2.15	103.7	1.53	3.17	2.05, 2.06	101.3	13.51
2 × J_{NNN}(M−O−F−M)	2.47	3.05,	74.5	3.02	5.22	2.80,	67.6	16.87
2 × J_a(M−F−M)	3.75	2.11, 2.15	123.1	5.56	3.58	2.02, 2.04	123.9	25.56
1 × J_b(M−O−M)	3.77	2.16, 2.16	121.9	9.72	3.75	2.09, 2.09	127.3	17.01
2 × J_{diag}(M−F−M)	3.84	2.11, 2.15	128.8	1.51	3.68	2.01, 2.06	129.8	-3.37_{FM}

[a] Interatomic distances, angles (SE), and dihedral angles (SSE) are also given.

we adopted the cycloidal description. The best refinement resulted in R_{magn} = 16.8%. The spin order consists of magnetic moments rotating mainly in the *ac* plane, along the incommensurate *a* axis. The phase between the two orbitals was refined to $[0.40(1)]\pi$. However, due to the nonzero imaginary M_y components (see Table 2), the spin precession follows a complex-cycloidal sequence along the incommensurate *a* axis, sketched in Figure 4e. Here, the cycloidal spin component within the *ac* plane is described by $M_{x\ max}$ = 1.82 μ_B and $M_{z,max}$ = 1.77 μ_B but oscillates around the equatorial *ac* plane by the sinusoidal M_y component scaled by $M_{y,max}$ = 0.6 μ_B. The final refinement of this model, leaving M_x, M_y, and M_z unconstrained as given in Table 2, gives a nearly constant Ni^{2+} moment with the average value 1.85 μ_B.

Frustration indexes of $|\Theta_{CW}|/T_N$ = 2.7 and 4.6 for $Mn_2(SeO_3)F_2$ and $Ni_2(SeO_3)F_2$, respectively, are in accordance with their refined magnetic structures. For the Ni compound for instance, one would expect next-neighbor (NN) AFM edge-sharing chains due to superexchange paths with an M−X−M angle >100° but frustration triggers a cycloidal magnetic structure. For $Ni^{2+}(d^8)$ vs $Mn^{2+}(d^5)$ cations the Goodenough−Kanamori rules may predict the main signs of superexchanges, at least for ideal 180 and 90° M−X−M interactions, but for intermediate values *ab initio* calculations generally prevail. Clearly for S = 5/2 spins, the chains are expected to be AFM for any angles and also by direct M−M t_{2g} overlap. In contrast for Ni^{2+} (S = 1), the interactions depend on the angle, while direct t_{2g}−t_{2g} interactions are inefficient.[27] The main identified magnetic exchanges, given in Table 3 and shown in Figure 2, show in the chains intermediate M−X−M angles of around 102°. They have been calculated using LDA +U, after mapping the total energies for a number of collinear spin configurations onto a classical Heisenberg model to yield individual exchange couplings for U = 4.6 eV[28] and the effective on-site exchange interaction J_{eff} = 1 eV. The calculated exchange strengths are scaled by the d(Ni−Ni) < d(Mn−Mn) interatomic distances returning the weakest J values for Mn^{2+} but are counterbalanced by the relative Ni^{2+} (S = 1) vs Mn^{2+} (S = 5/2) spin values, such that they finally order magnetically at similar Néel temperatures: i.e., T_N = 21.5 K (Ni) vs T_N = 26.5 K (Mn). Note that the set of calculated exchanges match rather well the Curie−Weiss temperature estimated in the mean field model $\Theta_{CW} = (1/3)\sum_i S(S+1)(J_i/k_B)$, giving calculated/experimental values of −95/−71 K and −88/−101 K for the Mn and Ni compounds, respectively.

The M−O−M exchange interactions J_O across the superexchange (SE) O−O bridge are antiferromagnetic in all cases but are also predominant over the J_F interactions in both compounds ($J_O/J_F \approx 1.8$), although the O electrons are covalently engaged in strong Se−O bonds, similarly to what is observed in $Fe(SeO_3)F$.[3] This superior magnetic connection not only is due to the scaling effect of the longer M−F bonds in comparison to M−O bonds[29] but also mainly stem from the O vs F electronegativity contrast, which favors the strongest electronic exchanges via oxygen media. Here, the weakest J values for the Mn^{2+} compound exclude a significant contribution of direct t_{2g}−t_{2g} exchanges via the shared edges expected in AFM for $Mn^{2+}(d^5)$ but inefficient for $Ni^{2+}(d^8)$. However, the diagonal J_{NNN} (NNN denotes the next-nearest neighbor) supersuperexchange in the edge-sharing chains is significant and destabilizes the AFM chains through strongly frustrated M_3 triangles along the zigzag chains. In addition, between the chains, the influence of exchange interaction J values should be considered not only by their values but also according to their occurrence, giving a key role to the interchain J_a and J_b SEs. They dictate the observed magnetic structures as follows. In the Mn case, they are largely predominant (~2−3 × $J_{in\text{-}chain}$) and the magnetic structure respects the $J_b > J_b > J_{diag}$ interplay. It returns ferromagnetic edge-sharing chains that are antiferromagnetically ordered between each other across the corner-sharing exchanges (see Figure 4a,b).

In addition, in this case the isotropic magnetic single ion Mn^{2+} (L = 0) serves in favor of a collinear magnetic structure commensurate with the crystallographic axis. This is the case here with spins oriented along the *a* axis that do not correspond to any local specific octahedral direction. In contrast, in the anisotropic Ni^{2+} ions with significant spin−orbit coupling (SOC) (μ_{eff} = 3.37 μ_B), the orientations of the magnetic moments are ruled by local orbital overlap, sometimes more prompt for spin wavelike features in which the spin orientation is held but its amplitude is modulated in the crystal. However, counter examples with rotating spins are common, including the spiral spin order of Fe^{3+} (L = 0) in $BiFeO_3$. In fact, the exact opposite situation in comparison to the title Mn/Ni pair has been reported in $Sr(Mn,Co)Ge_2O_6$ with a similar ferromagnetic zigzag chain with a collinear magnetic structure,[30] but in the Co^{2+} case there is strong SOC, while the Mn^{2+} (isotropic spin) compound develops a cycloidal spin configuration and spin-induced multiferroicity. It follows that the relative interplay of J values may on its own dictate the magnetic structure.[30] In $Ni_2(SeO_3)F_2$, the magnitudes of the interchain exchanges J_a and J_b are similar to those inside the edge-sharing chains, such that the frustration is destabilized into a cycloidal structure, keeping from site to site the main characteristic as for the Mn^{2+} case (see Figure 2d). In addition, the role of the weak ferromagnetic J_{diag} SSEs adds an extra degree of frustration in favor of the incommensurate magnetic period.

4. CONCLUSIONS

To summarize, $M_2(SeO_3)F_2$ ($M = Mn^{2+}, Ni^{2+}$), comprised of 1D-$[MO_2F_2]^{4-}$chains of edge-sharing octahedra with a rare topology of alternating O−O and F−F μ_2 bridges, were obtained as single crystals by an optimized hydrothermal route. Neutron diffraction experiments on powders indicate that $Mn_2SeO_3F_2$ exhibits a canted AFM ordering below 26 K with ferromagnetic chain units. Here the AFM ordering between them relies on predominant interchain interactions. In the isostructural $Ni_2SeO_3F_2$, the frustration is increased due to inter- and intrachain couplings on the same order of magnitude, promoting an incommensurate cycloidal magnetic structure below 21.5 K. While intuitively the significant SOC observed for Ni^{2+} may be a plausible crucial parameter in favor of the cycloidal state, the exact opposite situation found in the recent pyroxene compounds $SrMGe_2O_6$ with M = Co, Mn[30] emphasizes the relevant role of the sensitive nature of the magnetic ground state in topologies with apparently dominating low-dimensional units but complex overall exchange interplay. Further pushing this analogy allows the anticipation of type II multiferroicity, currently being tested for $Ni_2(SeO_3)F_2$.

■ ASSOCIATED CONTENT

Supporting Information

The Supporting Information is available free of charge at https://pubs.acs.org/doi/10.1021/acs.inorgchem.1c01074.

> Detailed experimental information, crystal data tables, magnetic structures, and DFT calculation methods (PDF)

Accession Codes

CCDC 2046139−2046140 contain the supplementary crystallographic data for this paper. These data can be obtained free of charge via www.ccdc.cam.ac.uk/data_request/cif, or by emailing data_request@ccdc.cam.ac.uk, or by contacting The Cambridge Crystallographic Data Centre, 12 Union Road, Cambridge CB2 1EZ, UK; fax: +44 1223 336033.

■ AUTHOR INFORMATION

Corresponding Authors

Olivier Mentré − *Université Lille Nord de France, UMR 8181 CNRS, Unité de Catalyse et de Chimie du Solide (UCCS USTL), F-59655 Villeneuve d'Ascq, France;* orcid.org/0000-0002-1822-6003; Email: olivier.mentre@univ-lille.fr

Minfeng Lü − *School of Environmental & Chemical Engineering, Jiangsu University of Science and Technology, Zhenjiang 212003 Jiangsu, Perople's Republic of China;* orcid.org/0000-0003-2576-3840; Email: m.f.lv@hotmail.com

Authors

Tianyu Zhu − *School of Environmental & Chemical Engineering, Jiangsu University of Science and Technology, Zhenjiang 212003 Jiangsu, Perople's Republic of China*

Haoming Yang − *School of Environmental & Chemical Engineering, Jiangsu University of Science and Technology, Zhenjiang 212003 Jiangsu, Perople's Republic of China*

Yong Jin − *School of Environmental & Chemical Engineering, Jiangsu University of Science and Technology, Zhenjiang 212003 Jiangsu, Perople's Republic of China*

Xinan Zhang − *School of Environmental & Chemical Engineering, Jiangsu University of Science and Technology, Zhenjiang 212003 Jiangsu, Perople's Republic of China*

Ángel M. Arévalo-López − *Université Lille Nord de France, UMR 8181 CNRS, Unité de Catalyse et de Chimie du Solide (UCCS USTL), F-59655 Villeneuve d'Ascq, France;* orcid.org/0000-0002-8745-4990

Clemens Ritter − *Institut Laue-Langevin, Grenoble Cedex, France*

Kwang-Yong Choi − *Department of Physics, Chung-Ang University, Seoul 06974, Republic of Korea;* orcid.org/0000-0001-8213-5395

Complete contact information is available at: https://pubs.acs.org/10.1021/acs.inorgchem.1c01074

Notes

The authors declare no competing financial interest.

■ ACKNOWLEDGMENTS

T.Z., H.Y., Y.J., X.Z., and M.L. acknowledge support from the National Natural Science Foundation of China (Award No.21671185). O.M. and A.M.A.-L. acknowledge support from the ANR (Grant ANR-16-CE08-0023) and the FEDER Région Hauts-de-France, and they also acknowledge the ILL for the allocated beamtime (DOI 10.5291/ILL-DATA.EASY-654) and the ILL Instrument Control Service for their support before and during the experiment. Claire Minaud is also thanked for experimental help. Finally for mixed anion compounds, the JSPS Core-to-Core Program (A) Advanced Research Network (JPJSCCA20200004) is also acknowledged as a source of motivation.

■ REFERENCES

(1) Kageyama, H.; Hayashi, K.; Maeda, K.; Attfield, J. P.; Hiroi, Z.; Rondinelli, J. M.; Poeppelmeier, K. R. Expanding frontiers in materials chemistry and physics with multiple anions. *Nat. Commun.* **2018**, *9*, 772.

(2) Zhang, D.; Berger, H.; Kremer, R.K.; Wulferding, D.; Lemmens, P.; Johnsson, M. Synthesis, Crystal Structure, and Magnetic Properties of the Copper Selenite Chloride $Cu_5(SeO_3)_4Cl_2$. *Inorg. Chem.* **2010**, *49*, 9683−9688.

(3) Hu, S.; Johnsson, M.; Law, J. M.; Bettis, J. L.; Whangbo, M.-H.; Kremer, R. K. Crystal Structure and Magnetic Propertiesof $FeSeO_3F$—alternating Antiferromagnetic S = 5/2 Chains. *Inorg. Chem.* **2014**, *53*, 4250−4256.

(4) Hu, S.; Johnsson, M. Synthesis and crystal structure of two synthetic oxofluoride framework compounds−$Co_2TeO_3F_2$ and $Co_2SeO_3F_2$. *Dalton Trans.* **2012**, *41*, 12786−12789.

(5) Mitoudi-Vagourdi, E.; Papawassiliou, W.; Mullner, S.; Jaworski, A.; Pell, A. J.; Lemmens, P.; Kremer.; et al. Synthesis and Physical Properties of the Oxofluoride $Cu_2(SeO_3)F_2$. *Inorg. Chem.* **2018**, *57*, 4640−4648.

(6) Tokura, Y.; Seki, S.; Nagaosa, N. Multiferroics of spin origin. *Rep. Prog. Phys.* **2014**, *77*, 076501.

(7) Jiang, J.; Zhu, B.; Zhu, T.; Yang, H.; Jin, Y.; Lü, M. Open-framework ammonium transition metal fluorophosphates with a Kagomé lattice network: synthesis, structure and magnetic properties. *Dalton Trans.* **2020**, *49*, 841−849.

(8) Jiang, J.; Lee, S.; Zhu, B.; Yu, Y.; Waerenborgh, J. C.; Choi, K.-Y.; Lü, M. Variable Dimensionality, Valence, and Magnetism in Fluoride-Rich Iron Phosphates $Ba_xFe_x(PO_4)F_y$ ($1 \le x \le 3, 2 \le y \le 12$). *Inorg. Chem.* **2019**, *58*, 133−142.

(9) Lü, M.; Jiang, J.; Zhu, B.; Zhao, Y.; Zhu, T.; Yang, H.; Jin, Y.; Kabbour, H.; Choi, K.-Y.; Harrison, W. T. A. Lone-pair self-containment in pyritohedron-shaped closed cavities: optimized

hydrothermal synthesis, structure, magnetism and lattice thermal conductivity of $Co_{15}F_2(TeO_3)_{14}$. *Dalton Trans.* **2020**, *49*, 2234−2243.

(10) Orive, J.; Balda, R.; Fernández, J.; Lezama, L.; Arriortua, M. I. Low temperature red luminescence of a fluorinated Mn-doped zinc selenite. *Dalton Trans.* **2013**, *42*, 12481−12494.

(11) Hu, S. *Transition metal oxofluorides comprising lone pair elements*. Doctoral Thesis; Stockholm University: Stockholm, 2014.

(12) *SAINT: Area-Detector Integration Software*; Siemens Industrial Automation, Inc.: Madison, WI, 1996.

(13) *SADABS: Area-Detector Absorption Correction*; Siemens Industrial Automation, Inc.: Madison, WI, 1995.

(14) Rodriguez-Carvajal, J. Recent advances in magnetic structure determination by neutron powder diffraction. *Phys. B* **1993**, *192*, 55.

(15) Koepernik, K.; Eschrig, H. Full-potential nonorthogonal local-orbital minimum-basis band-structure scheme. *Phys. Rev. B: Condens. Matter Mater. Phys.* **1999**, *59*, 1743.

(16) Perdew, J. P.; Wang, Y. Pair-distribution function and its coupling-constant average for the spin-polarized electron gas. *Phys. Rev. B: Condens. Matter Mater. Phys.* **1992**, *45*, 13244.

(17) Kresse, G.; Furthmüller, J. *Vienna Ab-initio Simulation Package (VASP)*; Institut für Materialphysik: Vienna, Austria, 2004.

(18) Kresse, G.; Furthmüller, J. Efficiency of ab-initio total energy calculations for metals and semiconductors using a plane-wave basis set. *Comput. Mater. Sci.* **1996**, *6*, 15; Efficient iterative schemes for ab initio total-energy calculations using a plane-wave basis set. *Phys. Rev. B: Condens. Matter Mater. Phys.* **1996**, *54*, 11169.

(19) Ellis, B. L.; Makahnouk, W. R. M.; Rowan-Weetaluktuk, W. N.; Ryan, D. H.; Nazar, L. F. Crystal Structure and Electrochemical Properties of A_2MPO_4F Fluorophosphates (A = Na, Li; M = Fe, Mn, Co, Ni). *Chem. Mater.* **2010**, *22*, 1059−1070.

(20) Brese, N. E.; O'Keeffe, M. Bond-valence parameters for solids. *Acta Crystallogr., Sect. B: Struct. Sci.* **1991**, *B47*, 192−197.

(21) Nelson, A. J.; Reynolds, J. G.; Roos, J. W. Core-level satellites and outer core-level multiplet splitting in Mn model compounds. *J. Vac. Sci. Technol., A* **2000**, *18*, 1072−1076.

(22) Carver, J. C.; Schweitzer, G. K.; Carlson, T. A. Use of X-Ray photoelectron spectroscopy to study bonding in Cr, Mn, Fe, and Co compounds. *J. Chem. Phys.* **1972**, *57*, 973.

(23) Oku, M.; Hirokawa, K.; Ikeda, S. X-ray photoelectron spectroscopy of manganese-oxygen systems. *J. Electron Spectrosc. Relat. Phenom.* **1975**, *7*, 465.

(24) Biesinger, M. C.; Lau, L. W. M. A.; Gerson, R.; Smart, R. St. C. The role of the Auger parameter in XPS studies of nickel metal,halides and oxides. *Phys. Chem. Chem. Phys.* **2012**, *14*, 2434−2442.

(25) Zhu, B.; Jiang, J.; Zhu, T.; Yang, H.; Jin, Y.; Choi, K.-Y.; Lü, M. Transition-Metal Monofluorophosphate $Ba_2M_2(PO_3F)F_6$ (M = Mn, Co, and Ni): Varied One-Dimensional Transition-Metal Chains and Antiferromagnetism. *Inorg. Chem.* **2020**, *59*, 3794−3804.

(26) Tang, Y.; Guo, W.; Zhang, S.; Yang, M.; He, Z. $M_3(TeO_3)(SO_4)(OH)_2\cdot 2H_2O$ (M = Ni, Co): Two Novel Quasi-2D Layered Tellurite-Sulfate Compounds with a Distorted Striped Kagomé Lattice. *Cryst. Growth Des.* **2014**, *14*, 5206−5211.

(27) Goodenough, J. B. *Magnetism and the Chemical Bond*; Wiley: New York, 1963.

(28) Trimarchi, G.; Wang, Z.; Zunger, A. Polymorphous band structure model of gapping in the antiferromagnetic and paramagnetic phases of the Mott insulators MnO, FeO, CoO, and NiO. *Phys. Rev. B: Condens. Matter Mater. Phys.* **2018**, *97*, 035107.

(29) Pedersen, K. S.; Sigrist, M.; Weihe, H.; Bond, A. D.; Thuesen, C. A.; Simonse, K. P.; Birk, T.; Mutka, H.; Barra, A.-L.; Bendix, J. Magnetic Interactions through Fluoride: Magnetic and Spectroscopic Characterization of Discrete, Linearly Bridged $[Mn^{III}_2(\mu\text{-}F)F_4(Me_3tacn)_2](PF_6)$. *Inorg. Chem.* **2014**, *53*, 5013−5019.

(30) Ding, L.; Colin, C. V.; Darie, C.; Bordet, P. $SrMGe_2O_6$ (M= Mn, Co): a family of pyroxene compounds displaying multiferroicity. *J. Mater. Chem. C* **2016**, *4*, 4236−4245.

https://doi.org/10.1021/acs.inorgchem.1c01074